

Vortex matching effects and flux dynamics manipulation in MgB_2 thin films via He-FIB-induced periodic artificial pinning centers

Ying Han(韩颖), Dali Yin(殷大利), Xinwei Cai(蔡欣炜), Yan Zhang(张焱), Yue Wang(王越), Lifeng Tian(田利丰), and Zizhao Gan(甘子钊)

Citation: Chin. Phys. B, 2026, 35 (**6**): 067405. DOI: 10.1088/1674-1056/ae3c8d
http://cpb.iphy.ac.cn; http://iopscience.iop.org/cpb

What follows is a list of articles you may be interested in

Fabrication and characterization of MgB_2 spherical shells with reduced thickness on 1 mm diameter Si_3N_4 spheres

Ruining Sun(孙瑞宁), Tiequan Xu(徐铁权), Yue Wang(王越), Furen Wang(王福仁), and Zizhao Gan(甘子钊)
Chin. Phys. B, 2025, 34 (**7**): 077402. DOI: 10.1088/1674-1056/adcdec

Half-integer Shapiro steps in MgB_2 focused He ion beam Josephson junctions

Dali Yin(殷大利), Xinwei Cai(蔡欣炜), Tiequan Xu(徐铁权), Ruining Sun(孙瑞宁), Ying Han(韩颖), Yan Zhang(张焱), Yue Wang(王越), and Zizhao Gan(甘子钊)
Chin. Phys. B, 2024, 33 (**8**): 087404. DOI: 10.1088/1674-1056/ad4d62

Co-doped $BaFe_2As_2$ Josephson junction fabricated with a focused helium ion beam

Ziwen Chen(陈紫雯), Yan Zhang(张焱), Ping Ma(马平), Zhongtang Xu(徐中堂), Yulong Li(李宇龙), Yue Wang(王越), Jianming Lu(路建明), Yanwei Ma(马衍伟), and Zizhao Gan(甘子钊)
Chin. Phys. B, 2024, 33 (**4**): 047405. DOI: 10.1088/1674-1056/ad21f7

Effects of irradiation on superconducting properties of small-grained MgB_2 thin films

Li Liu(刘丽), Jung Min Lee, Yoonseok Han, Jaegu Song, Chorong Kim, Jaekwon Suk, Won Nam Kang, Jie Liu(刘杰), Soon-Gil Jung, and Tuson Park
Chin. Phys. B, 2023, 32 (**12**): 127402. DOI: 10.1088/1674-1056/acf5d3

First-principles study of moderate phonon-mediated pairing in high-pressure monoclinic phase of BiS_2-based superconductors

Jie Cheng(程杰), Yu-Lan Cheng(程玉兰), Bin Li(李斌), and Sheng-Li Liu(刘胜利)
Chin. Phys. B, 2023, 32 (**10**): 107401. DOI: 10.1088/1674-1056/accd56

Vortex matching effects and flux dynamics manipulation in MgB_2 thin films via He-FIB-induced periodic artificial pinning centers

Ying Han(韩颖)[1], Dali Yin (殷大利)[1], Xinwei Cai(蔡欣炜)[1,†], Yan Zhang(张焱)[1,‡], Yue Wang(王越)[1], Lifeng Tian(田利丰)[2], and Zizhao Gan(甘子钊)[1]

[1] *Applied Superconductivity Center, State Key Laboratory for Mesoscopic Physics, School of Physics, Peking University, Beijing* 100871, *China*
[2] *Key Laboratory of Photochemical Conversion and Optoelectronic Materials, Technical Institute of Physics and Chemistry, Chinese Academy of Sciences, Beijing* 100190, *China*

(Received 23 November 2025; revised manuscript received 29 December 2025; accepted manuscript online 23 January 2026)

Flux dynamics, which describes the behavior of magnetic vortices in type-II superconductors, governs macroscopic electromagnetic properties of superconducting materials. Recently, cutting-edge approaches utilizing artificial periodic nanostructures for active control of the pinning centers help to deepen the understanding of relevant mechanisms of flux dynamics. This study demonstrates the controlled introduction of large-scale, periodic artificial pinning centers (APCs) in MgB_2 superconducting thin films to manipulate flux dynamics. Using focused helium ion beam (He-FIB) irradiation, we fabricated a square array of nanoscale columnar artificial pinning centers with a period of 100 nm on a 30 nm MgB_2 superconducting thin film. Magnetoresistance measurements near the critical temperature (T_c) reveal a pronounced vortex matching effect, evidenced by sharp resistance minima (dips) at specific integer and fractional magnetic matching fields. This effect is shown to be highly dependent on external parameters such as temperature, driving current, and the angle of the magnetic field. Furthermore, the large-area irradiation systematically suppresses T_c and broadens the superconducting transition of the film. This work establishes He-FIB as a potent tool for advanced flux pinning engineering and provides a comprehensive understanding of flux dynamics in superconductors with periodic pinning landscapes.

Keywords: vortex matching effects, periodic artificial pinning centers, MgB_2, focused helium ion beam

PACS: 74.25.Ha, 74.78.–w, 74.70.Ad, 41.85.Ar

DOI: 10.1088/1674-1056/ae3c8d **CSTR:** 32038.14.CPB.ae3c8d

1. Introduction

The application breakthrough of superconducting materials has always been limited by the energy loss caused by flux vortex motion and the rapid decay of critical current density in high magnetic fields. Flux dynamics is the theoretical basis for revealing this core issue. It systematically describes the nucleation and migration of flux vortices in superconductors under external magnetic fields and their dynamic interaction with defects, directly determining the macroscopic electromagnetic properties of superconducting materials.

Within the framework of flux dynamics, the pinning effect is a key means of suppressing flux flow: defects generate potential barriers in superconductors and hinder flux motion as pinning centers, thereby improving the in-field critical current density of materials. Although traditional random pinning, originating from defects such as point defects (impurities, vacancies, inclusions)[1–5] and one-dimensional defects (dislocations, irradiation tracks)[6–11] can enhance the pinning effect, the introduction of controlled, periodic artificial defects, serving as artificial pinning centers (APCs), can enable more precise manipulation of vortex behavior and thus lead to a deeper understanding of flux dynamics.

The emergence of artificial periodic pinning technology provides a promising avenue to overcome these limitations. By constructing periodic nanostructures through lithography, ion etching, self-assembly, and other methods, precise control over the spatial distribution of pinning centers is enabled.[12–21] The matching between the periodicity of the pinning centers and the flux lattice can significantly enhance the effective pinning force via the vortex matching effect, thereby achieving higher critical currents in different external magnetic fields. It has been established that parameters such as the periodic density, geometric morphology, and material composition critically influence superconducting performance by modulating dynamic processes such as flux creep and depinning thresholds.[22–29] However, a comprehensive understanding of flux dynamics under complex multi-field coupling conditions, as well as the quantitative structure–performance correlation, remains elusive.

Recently, advanced fabrication methods like He-FIB have garnered significant interest for creating artificial periodic structures in superconductors.[30–34] Unlike conventional ion irradiation techniques that require pre-fabricated physical masks, He-FIB employs a focused helium ion beam for maskless direct-write patterning. Its resolution can easily

†Corresponding author. E-mail: xwcai@pku.edu.cn
‡Corresponding author. E-mail: zhang_yan@pku.edu.cn

© 2026 Chinese Physical Society and IOP Publishing Ltd. All rights, including for text and data mining, AI training, and similar technologies, are reserved.

achieve sub-10–20 nm, far surpassing traditional lithography and even some masked ion irradiation techniques.[35–42] This high resolution enables the fabrication of artificial pinning arrays with lattice constants below 100 nm, where pronounced vortex matching effects are readily observable. Notably, Karrer *et al.*[30] recently demonstrated a 20 nm periodic pinning array exhibiting vortex matching at 6 T. Additionally, by tuning the helium ion energy and dose, the penetration depth and defect density in the superconducting film can be precisely modulated.[43–46] This advanced technique represents a significant leap forward in the nanoscale engineering of flux pinning landscapes, pushing the boundaries of vortex control. Employing the He-FIB technique to introduce periodic APCs has been extensively researched, but reports on MgB_2 featuring two-band superconductivity are scarce, especially with He-FIB precision.

In this study, we employ focused He ion beam microscopy to fabricate artificial periodic defect arrays in MgB_2 thin films. We first observe integer and fractional matching effects and systematically investigate the influence of temperature, applied current, and the angle of the magnetic field on vortex dynamics. Our work addresses key questions, including the mechanism by which fractional matching enhances pinning in MgB_2, the interplay between defect geometry and vortex dynamics, and the potential for designing improved superconducting devices. This research not only advances our fundamental understanding of flux pinning but also contributes to the development of more efficient superconducting applications.

2. Methods

High-quality MgB_2 thin films ($\sim$ 30 nm) were epitaxially grown on SiC (0001) substrates via hybrid physical–chemical vapor deposition (HPCVD). Subsequently, bilayers of Ti/Ag (5 nm/200 nm) were deposited by direct current (DC) magnetron sputtering as electrical bonding pads. During metal deposition, a physical shadow metal mask was employed to expose the microbridge regions intended for subsequent irradiation and patterning, thereby avoiding unwanted metal deposition and ensuring a clean interface.

The microbridges were then patterned using standard ultraviolet (UV) lithography followed by argon (Ar) ion milling. The defined microbridges were subsequently processed using a helium ion microscope: large-area irradiation was performed using the area patterning mode, while square arrays of columnar defects (CDs) with a $\sim$ 100 nm period were fabricated via the point scanning mode. Detailed processing parameters are provided in the next section.

The surface morphology, structural integrity, and irradiated regions of the fabricated MgB_2 microbridges were comprehensively characterized using multiple microscopy techniques. Initially, the microbridges were examined with an optical microscope (Olympus BH2) to obtain a general overview. Subsequently, to obtain detailed morphology information and edge details of the microbridges, imaging was performed with a scanning electron microscope (SEM) (Nova NanoSEM 430). Furthermore, a helium ion microscope (HIM, Carl Zeiss Orion NanoFab) was utilized to achieve high-resolution imaging of surface defects and the patterned nanoscale structures.

The electrical transport properties of the microbridges were characterized using a physical property measurement system (PPMS) with a maximum magnetic field of 9 T. Resistance measurements were carried out using the standard four-probe technique. A Keithley model 2400 sourcemeter and a Keithley model 2182A nanovoltmeter were used as the external current source and voltmeter, respectively. Angle-dependent resistance measurements were performed using a horizontal rotator installed in the PPMS.

3. Results and discussions

Figure 1(a) is a schematic diagram of the irradiation method. Targeted irradiation was performed using a Carl Zeiss Orion NanoFab helium ion microscope with 30 keV beam energy to ensure sufficient penetration depth throughout the entire MgB_2 film. A low beam current of 1–2 pA was employed to minimize space-charge effects[47] and to achieve a highly focused probe, thereby enabling precise nanoscale patterning and minimizing unintended lateral damage.[48,49] The pattern was precisely aligned to cover the entire active area of the MgB_2 microbridge between the voltage probes shown in Figs. 1(b) and 1(c), ensuring that the measured transport properties are solely influenced by the modified region.

Under backlight illumination, the overall morphology of the microbridge and the SiC substrate is clearly visible in Fig. 1(b). The irradiated region exhibits a significant and uniform contrast change compared to the surrounding pristine MgB_2. As is well known, darkening usually corresponds to a decrease in transmittance or an enhancement in light scattering. This indicates that after high-dose helium ion irradiation, high densities of point defects, displacement damage, and potential voids/bubbles are introduced into MgB_2, leading to amorphization and increased surface roughness.[50] These effects significantly enhance light scattering and absorption, reducing the intensity of transmitted light. As a result, a darkened contrast is observed under the optical microscope in backlight mode. In Fig. 1(c), at very high doses (e.g., 200 ions/nm^2), the irradiated region exhibits "whitening" (i.e., brighter contrast) under SEM imaging. In SEM, the brightness (signal intensity) of a region primarily depends on the number of secondary electrons (SE) emitted from that area. The greater the emission of secondary electrons, the brighter the region appears in the image. Typically, for conductive samples,

higher electrical resistance generally corresponds to darker regions in the SEM image. However, in our experiments, it was observed that the electrical resistance of MgB_2 increased after irradiation, as evidenced by the *R*–*T* curve in Fig. 1(d). This observation deviates from the general expectation that higher resistance leads to darker contrast. A plausible explanation for the morphology change is hillock formation.[51,52] According to Kasaei's work,[51] He ions can remain in the substrate and cause swelling, leading to the formation of small hills with heights up to 30 nm. These raised regions tend to emit more secondary electrons under electron beam bombardment, resulting in a stronger signal and a brighter appearance in the image.

The superconducting transition, measured by resistivity versus temperature (*R*–*T*) in Fig. 1(d), shows a systematic degradation with increasing dose. With increasing irradiation dose (from 0 to 100 ions/nm^2), the critical temperature (T_c) shows a systematic and notable suppression, decreasing from approximately 40.7 K (pristine sample) to about 21.7 K (100 ions/nm^2). Concurrently, the transition width broadens, indicating reduced sample homogeneity and degraded superconducting properties after irradiation. At higher doses (200 ions/nm^2), superconductivity is completely suppressed, resulting in a finite residual resistance of approximately 1.7 Ω at 2 K.

These observations can be attributed to the introduction of non-magnetic defects by He ions, which act as pair-breaking centers in the MgB_2 lattice, thereby suppressing the superconducting order parameter in accordance with Anderson's theory for dirty superconductors.[53] Further studies, including transmission electron microscopy (TEM), Raman spectroscopy, x-ray diffraction, first-principles calculations, and molecular dynamics simulations, could help to elucidate the exact nature of these defects and their spatial distribution.

The pre-patterned MgB_2 microbridges are loaded into the helium ion microscope. Using a low ion fluence, the sample surface is first properly aligned to the focal plane of the ion optics. Controlled defocus is achieved by increasing the working distance by 10 μm from the focal plane, resulting in irradiation spots approximately 20 nm in diameter. Each point is irradiated with 30 keV He^+ ions using a dwell time of 20 s and a beam current of 1.4 pA. This corresponds to a fluence of 1.8×10^5 He^+ ions per point. The total effective irradiated area is approximately 30 μm × 16 μm as depicted in the inset of Fig. 2(a). The spacing between adjacent points is determined by the scanning step of the focused He ion beam.

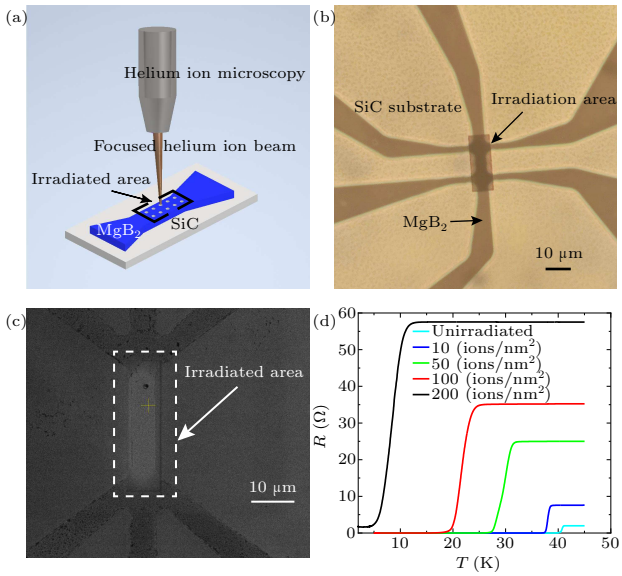


Fig. 1. Influence of helium ion irradiation on the morphological and superconducting properties of MgB_2 thin films. (a) Schematic diagram of the periodic defect array fabrication via focused He-ion beam irradiation. (b) Optical microscope image of the irradiated microbridge under backlight illumination. (c) Large-field-of-view SEM image of the MgB_2 microbridge structure after He-ion irradiation with a dose of 200 ions/nm^2. (d) Resistance as a function of temperature (*R*–*T*) for the MgB_2 samples irradiated with various doses of He ions.

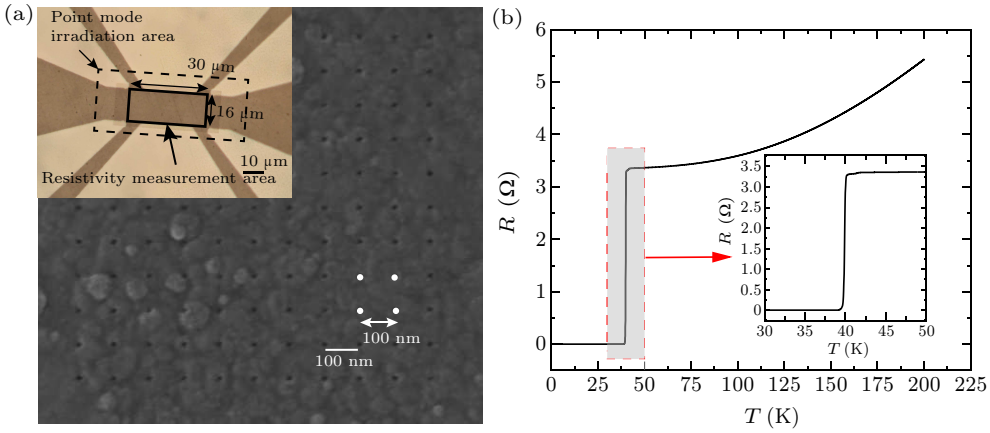


Fig. 2. (a) Helium ion microscope image of the periodic nanoscale pinning array structure with a 100 nm period. The upper-left inset shows an optical image under backlight illumination of the irradiated area marked with a dashed-line box and the active measurement region marked with a solid box. (b) Resistance as a function of temperature (*R*–*T*) for a MgB_2 microbridge with a periodic defect array of 100 nm period. The inset shows an enlarged view of the gray boxed region indicating the superconducting transition.

The high-resolution He-ion microscope image in Fig. 2(a) clearly reveals the nanoscale dot array within the irradiated region. Note that a dwell time of 1 s was used instead of the nominal experimental dwell time of 20 ms for a clearly visible nanohole image. The image shows a uniform hole size of about 20 nm and a highly periodic, ordered lattice spacing of 100 nm. This directly demonstrates the exceptional capability of the He-ion microscope for precision nanofabrication and defect engineering. Through this technique, highly tunable artificial pinning centers (APCs) can be introduced into the superconductor. These periodically arranged defects can exert strong pinning forces on flux vortices, thereby potentially enhancing the field-dependent critical current density (J_c) without severely degrading the superconducting transition temperature (T_c). As shown in Fig. 2(b), the critical temperature of the microbridge is 39.9 K and the transition width is 1.23 K, indicating that the He-FIB fabrication process successfully creates a periodic array of APCs without inducing significant degradation of the intrinsic superconducting properties of the MgB_2 film.

The flux matching effect, also referred to as the commensurability effect, predicts that when the external magnetic field satisfies certain integer or fractional ratios between the vortex density and the APC density, the vortices are pinned at the most stable positions, forming a coherent superlattice. This effect occurs at specific applied magnetic fields known as matching fields.

For a square array with periodicity a, the n-th matching field B_n is given by

$$B_n = n\frac{\Phi_0}{A} = n\frac{\Phi_0}{a^2}, \tag{1}$$

where n is an integer or fractional number of vortices contained within the unit cell of the square pinning array with area $A = a^2$. B_1 corresponds to the first matching field, where the vortex density equals the pinning site density. When the magnetic field $B > B_1$, one of two scenarios may occur: either some or all APCs are filled with multiquanta vortices when the APC radius is larger than the coherence length, or interstitial vortices enter between the APCs.

Some representative stable configurations are illustrated in Fig. 3(b). The most important case is the first matching field, B_1, where the number of vortices exactly equals the number of pinning sites. At this field, each pinning center captures a single vortex, forming a highly ordered and stable configuration that maximizes the pinning force and minimizes vortex motion, leading to a deep minimum in resistance. Similar commensurability effects can also be observed at fractional (e.g., $B_1/2$, $B_1/3$, $B_1/4$) and integer multiples (e.g., $2B_1$, $3B_1$) of the first matching field. In studies of critical currents and vortex states in superconductors with periodic pinning, numerical simulations[12,16,54] and imaging experiments[20] have revealed distinct vortex configurations at integer and fractional matching fields. For square pinning arrays, ordered vortex lattices form at fillings of $n = 1$ (fully occupied square grid), $n = 1/2$ (checkerboard pattern with alternating occupied and empty sites), $n = 1/3$ (imperfect diagonal stripe patterns), and $n = 2/3$ (complementary stripe pattern to $n = 1/3$). At these fields, more complex yet still ordered vortex configurations, such as multi-vortex superlattices, are formed, which also lead to local enhancements in pinning efficiency.

The fractional flux matching effect observed in experiments may be attributed to the presence of fractional vortices[55–58] in two-band superconductors such as MgB_2. In multiband systems, owing to weak interband coupling, fractional vortices — each carrying a fraction of the standard flux quantum Φ_0 — can form and stabilize in periodic pinning arrays[56] or along linear normal strips[57] under specific circumstances. This leads to matching phenomena at fractional fields, where dissociated vortices align with pinning sites, manifesting as peaks in the critical current or as self-induced Shapiro steps in I–V curves.[56]

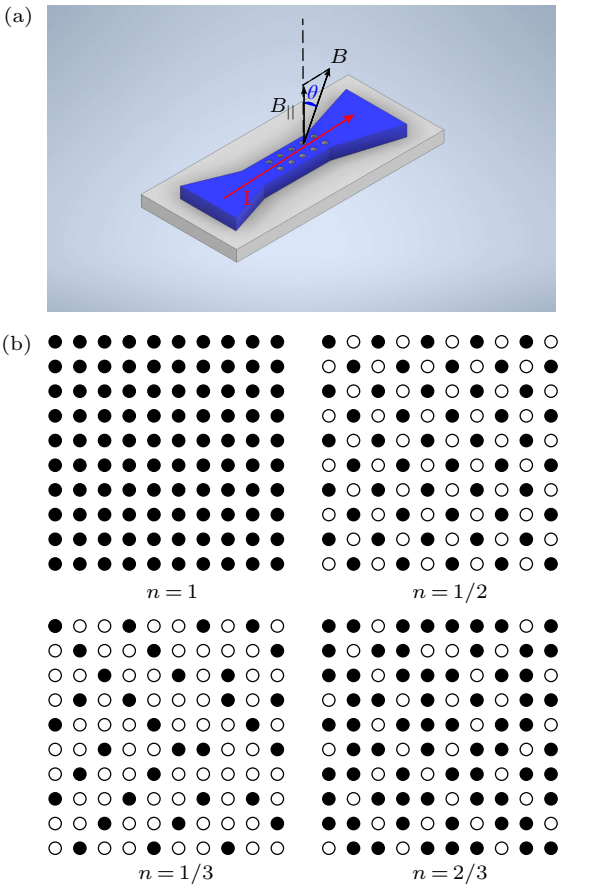


Fig. 3. (a) Schematic diagram of the experimental measurement setup. An external current I is applied, and the resulting voltage V is measured. A uniform external magnetic field $\boldsymbol{B}$ is applied, denotes the orientation between the magnetic field direction $\boldsymbol{B}$ and the film normal. The parallel component $B_{\parallel}$ is defined as $B_{\parallel} = B\cos(\theta)$. (b) Schematic diagram of stable configurations of flux vortices in a superconducting thin film with a square periodic array of APCs under different applied magnetic fields. APCs are represented as empty circles, and vortices are represented as solid black circles.

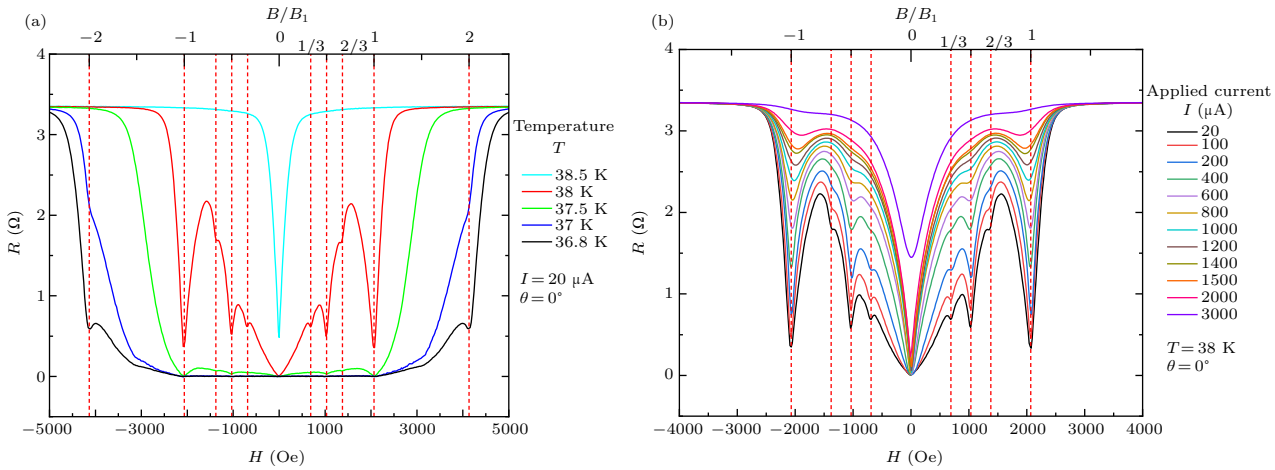


Fig. 4. (a) Resistance as a function of magnetic field (R–H) curves measured at different temperatures near the superconducting transition temperature (T_c) for an MgB_2 thin film patterned with a 100 nm-period nanohole array fabricated by helium ion microscopy. All curves were measured under a constant applied current of 20 μA. (b) Resistance as a function of magnetic field (R–H) curves measured under different applied transport currents ranging from 20–3000 μA. All curves were measured at a fixed temperature of 38 K.

An alternative explanation involves interstitial pinning.[15,59,60] In superconductors with periodic pinning arrays, interstitial pinning, wherein vortices are located in the regions between designated pinning sites rather than the sites themselves, serves as a key mechanism underlying fractional matching effects. Under the condition of weak pinning strength, some vortices are directly trapped at the artificial defects, while others occupy the interstitial spaces between defects at certain fractional fields. These interstitial vortices are effectively immobilized by the strong repulsion from the directly pinned vortices. This indirect interstitial pinning suppresses vortex creep, leading to the observed resistance dips.

At these specific matching fields, the pinning force reaches a maximum, vortex motion is strongly inhibited, and a pronounced minimum in resistance is observed macroscopically. Therefore, we conducted experiments to investigate the vortex matching effects in our samples.

As shown in Fig. 4(a), the most prominent features are the sharp resistance dips that occur at specific, well-defined matching magnetic fields. This behavior is a direct signature of the artificial periodic pinning landscape and is fundamentally different from the smooth R–H curves observed in conventional superconductors or films with random disorder.[61]

The resistance dips do not appear at all temperatures; their presence and amplitude are strongly temperature-dependent. At higher temperatures (38.5 K), the R–H curve shows only a dip at 0 Oe and tends toward a constant value under relatively higher magnetic fields with no observable matching features. At intermediate temperatures, such as 38 K, the dips emerge and become sharp and deep. Multiple dips at various integer and fractional matching fields become clearly visible. The data allow identification of both fractional ($n = 1/3$, 1/2, 2/3) and integer ($n = 1$) matching fields. At lower temperatures, the dips, while perhaps still present, weaken, broaden, or disappear entirely. The entire R–H curve flattens near zero resistance over a wide field range. At 37.5 K, only dips at the $n = 1/2$ fractional matching field and the $n = 1$ integer matching field are observed, with dips becoming quite broad and shallow compared with those at 38 K. At 37 K, only a small dip at $n = 2$ is present, whereas at 36.8 K, the dip at $n = 2$ becomes deeper.

The temperature dependence of the resistance dips stems from the competition among three competing energy scales: thermal fluctuations, an artificial pinning potential, and intrinsic pinning strength.[62–64] At higher temperatures (38.5 K), thermal fluctuations dominate. The thermal energy is high enough to disrupt the binding of vortices to the pinning sites and to melt the ordered vortex lattice. Vortices are in a disordered vortex liquid state where the subtle ordering effect of the periodic array is overwhelmed by thermal noise. Hence, no matching effects are observed. As the temperature decreases, thermal fluctuations are reduced, allowing the ordering influence of the periodic array to dominate. At the matching fields, the system achieves a highly stable, ordered vortex configuration with minimal energy, leading to maximal suppression of vortex motion and the characteristic sharp, negative dips. At very low temperatures, the intrinsic pinning strength from inherent defects or material properties becomes dominant. Vortices are pinned so effectively everywhere that the additional benefit of periodic matching becomes negligible. The system enters a collective pinning regime where the resistance is zero across a wide field range, masking the unique signature of the artificial array.

The magnetoresistance (R–H) of the MgB_2 thin film is measured in Fig. 4(b) under different applied currents to systematically investigate the influence of the driving current density on the flux vortex dynamics in a periodic pinning array. As shown in Fig. 4(b), with increasing transport current, the

resistance dips at the integer ($n = 1$) and fractional matching fields ($n = 1/3$, 1/2, 3/2) exhibit systematic broadening and a reduction in amplitude. Under relatively high current conditions, the dips almost disappear, indicating that the matching effect is almost completely obscured. The *R*–*H* curves exhibit perfect mirror symmetry, $R(+H) = R(-H)$, indicating that the resistance depends strictly on the magnitude of the magnetic field rather than its direction. The overall resistance level increases with current, indicating enhanced dissipation from the flow of unpinned flux vortices.

Upon close inspection, the positions of the matching dips (e.g., the $n = 1/2$ and $n = 1$ dips) show a slight shift toward lower magnetic fields as the current increases. A possible explanation is that the current flowing through the microbridge generates its own magnetic field, which superimposes with the externally applied magnetic field, thereby slightly altering the effective total field acting on the vortices. For our square defect pinning array geometry, this self-field may partially superimpose on the external field, leading to a slight reduction in the required external field to achieve the same matching condition.

An additional mechanism involves elastic deformation of the vortex lattice induced by the increasing Lorentz force prior to depinning.[12,54,65–68] As the transport current increases, the Lorentz force exerts shear or compressive stress on the lattice, leading to distortions in intervortex spacing and lattice symmetry. These deformations can alter the effective matching condition, allowing commensurability features to manifest at lower external fields, as the distorted lattice accommodates the periodic pinning array more readily even under mismatch.

From Fig. 5(a), as the tilt angle (θ) increases, the entire resistance curve shifts toward higher magnetic fields, resulting in different matching magnetic fields for different curves. After transforming the *x*-axis from the total external field ($\boldsymbol{H}$) to its component parallel to the *c*-axis of the sample ($H_{\parallel} = H\cos(\theta)$), the resistance dips for the *R*–$H_{\parallel}$ curves at all angles return to the original positions where $n = 1/3$, 1/2, 2/3 fractional and $n = 1$ integer matching fields can be identified. This scaling behavior validates the angular dependence of the magnetic field matching effect in our periodic defect pinning arrays. The vortex matching effect is primarily determined by the vortex components parallel to the columnar defects (CDs), as this component dictates the interaction with the in-plane periodic pinning array.[31,68]

As the angles increase, the resistance dips become broader and shallower. At very large angles (e.g., $\theta = 70^{\circ}$), the matching effect is significantly suppressed and the dips nearly vanish. Although the magnetic field perpendicular to the sample surface remains the same at each matching field, the total magnetic field increases with the angle. This introduces a magnetic field component that is perpendicular to the surface of the sample. Artificial periodic defects are most effective when vortices are straight and aligned along the defect axes. Tilted vortices interact less with these fixed-geometry pinning centers, weakening the commensurability between the vortex lattice and the pinning array. This leads to broader and shallower dips in *R*–*H* curves.

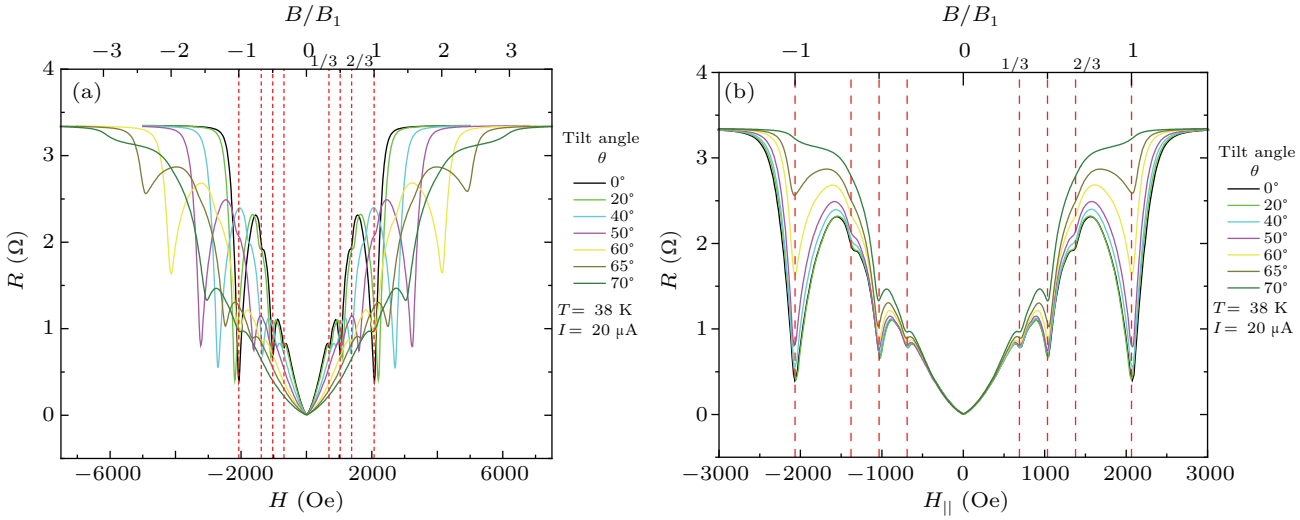


Fig. 5. (a) Resistance as a function of magnetic field (*R*–*H*) measured at different tilt angles between the applied magnetic field $\boldsymbol{H}$ and the direction perpendicular to the sample surface. (b) Resistance as a function of the parallel component of the magnetic field (*R*–$H_{\parallel}$). All curves were measured at a fixed temperature of 38 K.

4. Conclusion and perspectives

In this study, we successfully achieved large-area irradiation of MgB_2 superconducting thin films and fabricated artificial pinning arrays with a period of 100 nm using a focused helium ion beam (He-FIB) technique. Furthermore, we systematically explored the resulting vortex matching effects and their dependence on external parameters.

Large-area helium ion irradiation significantly altered the intrinsic superconducting properties of the film. The T_c was systematically suppressed, and the transition width broadened

considerably with increasing irradiation doses. This indicates that the irradiation introduced uniformly distributed lattice disorder, reducing sample homogeneity and leading to amorphization at high doses.

MgB_2 thin films with 100 nm APC arrays were fabricated by He-FIB. We successfully observed the vortex matching effects, manifested as sharp resistance dips at specific integer and fractional matching magnetic fields (e.g., $\boldsymbol{B}_1$, $\boldsymbol{B}_{1/2}$, $\boldsymbol{B}_{1/3}$, $\boldsymbol{B}_{2/3}$, $\boldsymbol{B}_2$) in the *R*–*H* curves. These features originate from the commensurability between the vortex lattice and the periodic pinning array. The prominence of this matching effect exhibits a strong dependence on temperature, driving current, and magnetic field angle.

The matching effect is most pronounced within a specific temperature window. Thermal fluctuations disrupt vortex order near T_c, while the dominance of intrinsic pinning at very low temperatures masks the modulation effect of the periodic array.

Increasing the applied transport current leads to broadening, shallowing, and even shifting of the matching dips. This behavior arises because the self-field generated by the current slightly modifies the effective magnetic field, and the increased Lorentz force promotes vortex depinning, thereby weakening the flux matching effect.

The flux matching effect exhibits pronounced anisotropy. When the magnetic field is perpendicular to the surface of the sample, the vortex matching effect is the most prominent, and resistance dips are the sharpest. For tilted magnetic fields, the perpendicular field component is the sole physical parameter governing the flux matching effect. In contrast, the parallel field component degrades pinning efficiency by inducing vortex tilting.

While our experimental results provide valuable insights into vortex dynamics in this system, several avenues remain for further exploration. In particular, more in-depth and comprehensive simulation work, such as time-dependent Ginzburg–Landau (TDGL) modeling, could elucidate the microscopic vortex configurations at fractional matching fields. This would complement our observations and offer predictive insights for optimizing pinning landscapes in MgB_2 and other multi-band superconductors. Future studies could also extend to varying lattice geometries or hybrid pinning strategies to enhance critical currents for practical applications.

In summary, this work demonstrates the efficacy of He-FIB as a powerful nanofabrication technique for introducing controllable, large-area artificial pinning centers in superconducting films. Furthermore, it provides a comprehensive understanding of flux dynamics in a periodic pinning system through a multi-parameter investigation. These findings offer crucial guidance for the future design of high-performance superconducting devices intended for operation under complex conditions.

Acknowledgments

Project supported by the National Natural Science Foundation of China (Grant No. 12104016), the Natural Science Foundation of Beijing, China (Grant No. 2244106), the National Key Research and Development Program of China (Grant Nos. 2020YFF01014706 and 2021YFB3800201), and the Peking University Funding on "Instrument Innovation and Key Technology R&D" (Grant No. 2024).

References

[1] Yuan L K, Weng T Q, Ke C, Cheng C H and Zhao Y 2025 *J. Alloys Compd.* **1016** 179004
[2] Pint W and Schachinger E 1989 *Physica C* **159** 33
[3] Wu Z P, Sun Y, Durajski A P, Zheng F, Antropov V, Ho K M and Wu S Q 2023 *Phys. Rev. Mater.* **7** L101801
[4] Li W X, Kang J X, Fu S W, Hu Y M, Hu P F, Zhu M Y and Li Y 2019 *J. Rare Earths* **37** 124
[5] Kimber S A J, Kreyssig A, Zhang Y Z, Jeschke H O, Valentí R, Yokaichiya F, Colombier E, Yan J, Hansen T C, Chatterji T, McQueeney R J, Canfield P C, Goldman A I and Argyriou D N 2009 *Nat. Mater.* **8** 471
[6] Timmons E I, Teknowijoyo S, Kończykowski M, Cavani O, Tanatar M A, Ghimire S, Cho K, Lee Y, Ke L, Jo N H, Bud'ko S L, Canfield P C, Orth P P, Scheurer M S and Prozorov R 2020 *Phys. Rev. Res.* **2** 023140
[7] Taen T, Nakajima Y, Tamegai T and Kitamura H 2012 *Phys. Rev. B* **86** 094527
[8] Haberkorn N, Kim J, Gofryk K, Ronning F, Sefat A S, Fang L, Welp U, Kwok W K and Civale L 2015 *Supercond. Sci. Technol.* **28** 055011
[9] Erdem O and Yanmaz E 2017 *J. Supercond. Nov. Magn.* **30** 769
[10] Tarantini C, Aebersold H U, Bernini C, Braccini V, Ferdeghini C, Gambardella U, Lehmann E, Manfrinetti P, Palenzona A, Pallecchi I, Vignolo M and Putti M 2007 *Physica C* **463–465** 211
[11] Ferrando V, Pallecchi I, Tarantini C, Marré D, Putti M, Ferdeghini C, Gatti F, Aebersold H U, Lehmann E, Haanappel E, Sheikin I, Orgiani P and Xi X X 2007 *J. Appl. Phys.* **101** 043903
[12] Reichhardt C and Grønbech-Jensen N 2001 *Phys. Rev. B* **63** 054510
[13] Ooi S, Mochiku T and Hirata K 2009 *Physica C* **469** 1113
[14] Ooi S, Mochiku T and Hirata K 2010 *Physica C* **470** S868
[15] Ooi S, Mochiku T and Hirata K 2009 *J. Phys.: Conf. Ser.* **150** 052203
[16] Sabatino P, Cirillo C, Carapella G, Trezza M and Attanasio C 2010 *J. Appl. Phys.* **108** 053906
[17] Cao R, Horng L, Wu J C, Yang T J and Wu T C 2010 *J. Supercond. Nov. Magn.* **23** 1051
[18] Haag L T, Zechner G, Lang W, Dosmailov M, Bodea M A and Pedarnig J D 2014 *Physica C* **503** 75
[19] Kamran M, Anis-ur-Rehman M, Mansoor K, He S K and Qiu X G 2011 *J. Supercond. Nov. Magn.* **24** 919
[20] Field S B, James S S, Barentine J, Metlushko V, Crabtree G, Shtrikman H, Ilic B and Brueck S R J 2002 *Phys. Rev. Lett.* **88** 067003
[21] Thakur A D, Ooi S, Chockalingam S P, Jesudasan J, Raychaudhuri P and Hirata K 2009 *Appl. Phys. Lett.* **94** 262501
[22] Coskun E 1999 *Appl. Math. Comput.* **106** 31
[23] Andry K 2013 *Controlling the Flux Dynamics in Superconductors by Nanostructured Magnetic Arrays* (Ph.D. dissertation) (Antwerp: University of Antwerp)
[24] Reichhardt C and Grønbech-Jensen N 2001 *Phys. Rev. B* **63** 054510
[25] Vizarim N P, Carlone M, Verga L G and Venegas P A 2017 *Mat. Res.* **20** 899
[26] Tanaka Y, Yanagisawa T, Crisan A, Shirage P M, Iyo A, Tokiwa K, Nishio T, Sundaresan A and Terada N 2011 *Physica C* **471** 747
[27] Baert M, Metlushko V V, Jonckheere R, Moshchalkov V V and Bruynseraede Y 1995 *Europhys. Lett.* **29** 157
[28] Chen C, Liu Y, Chen Y, Hu Y N, Zhang T Z, Li D, Wang X, Wang C X, Lu Z Y W, Zhang Y H, Zhang Q L, Dong X L, Wang R, Feng D L and Zhang T 2024 *Phys. Rev. X* **14** 041039
[29] Cuppens J, Ataklti G W, Gillijns W, Van De Vondel J, Moshchalkov V V and Silhanek A V 2011 *J. Supercond. Nov. Magn.* **24** 7

[30] Karrer M, Aichner B, Wurster K, Magén C, Schmid C, Hutt R, Budinská B, Dobrovolskiy O V, Kleiner R, Lang W, Goldobin E and Koelle D 2024 *Phys. Rev. Appl.* **22** 014043

[31] Aichner B, Backmeister L, Karrer M, Wurster K, Kleiner R, Goldobin E, Koelle D and Lang W 2023 *Condens. Matter* **8** 32

[32] Emmrich D, Beyer A, Nadzeyka A, Bauerdick S, Meyer J C, Kotakoski J and Gölzhäuser A 2016 *Appl. Phys. Lett.* **108** 163103

[33] Xia D, Huynh C, McVey S, Kobler A, Stern L, Yuan Z and Ling X S 2018 *Nanoscale* **10** 5198

[34] Aichner B, Müller B, Karrer M, Misko V R, Limberger F, Mletschnig K L, Dosmailov M, Pedarnig J D, Nori F, Kleiner R, Koelle D and Lang W 2019 *ACS Appl. Nano Mater.* **2** 5108

[35] Allen F I 2021 *Beilstein J. Nanotechnol.* **12** 633

[36] Hill R and Rahman F 2011 *Nucl. Instrum. Methods Phys. Res. A* **645** 96

[37] Petrov Y V, Grigoryev E A and Baraban A P 2020 *Nanotechnology* **31** 215301

[38] Hlawacek G and Gölzhäuser A 2016 *Helium Ion Microscopy* (Cham: Springer International Publishing) pp. 415–445

[39] Yin D L, Cai X W, Xu T Q, Sun R L, Han Y, Zhang Y, Wang Y and Gan Z Z 2024 *Chin. Phys. B* **33** 087404

[40] Yin D L, Cai X W, Xu T Q, Sun R L, Chen Z W, Han Y, Tian L F, Wang Y, Zhang Y and Gan Z Z 2024 *Physica C* **623** 1354532

[41] Chen Z W, Zhang Y, Ma P, Xu Z T, Li Y L, Wang Y, Lu J M, Ma Y W and Gan Z Z 2024 *Chin. Phys. B* **33** 047405

[42] Chen Z W, Li Y L, Zhu R, Xu J, Xu T Q, Yin D L, Cai X W, Wang Y, Lu J M, Zhang Y and Ma P 2022 *Chin. Phys. Lett.* **39** 077402

[43] Cybart S A, Cho E Y, Wong T J, Wehlin B H, Ma M K, Huynh C and Dynes R C 2015 *Nat. Nanotechnol.* **10** 598

[44] Cho E Y, Zhou Y W, Cho J Y and Cybart S A 2018 *Appl. Phys. Lett.* **113** 022604

[45] Kasaei L, Melbourne T, Manichev V, Feldman L C, Gustafsson T, Chen K, Xi X X and Davidson B A 2018 *AIP Advances* **8** 075020

[46] Emmrich D, Beyer A, Nadzeyka A, Bauerdick S, Meyer J C, Kotakoski J and Gölzhäuser A 2016 *Appl. Phys. Lett.* **108** 163103

[47] Böer K W 2010 *Introduction to Space Charge Effects in Semiconductors* (Vol. 160) (Berlin, Heidelberg: Springer Berlin, Heidelberg) pp. 15–40

[48] Li Z P, Ma H Q, Huang J W, Liu Y Q, Shao M X, Luo Z Y, Du X C, Wu C Y, Li N N, Wang H B and Li P 2024 *Supercond. Sci. Technol.* **37** 125010

[49] Townsend P D 1987 *Rep. Prog. Phys.* **50** 501

[50] Kasaei L, Manichev V, Li M, Feldman L C, Gustafsson T, Collantes Y, Hellstrom E, Demir M, Acharya N, Bhattarai P, Chen K, Xi X X and Davidson B A 2019 *Supercond. Sci. Technol.* **32** 095009

[51] Leclerc S, Declémy A, Beaufort M F, Tromas C and Barbot J F 2005 *J. Appl. Phys.* **98** 113506

[52] Anderson P W 1959 *J. Phys. Chem. Solids* **11** 26

[53] Liao H Y, Zhou S P, Shi X Y and Zhu B H 2003 *Phys. Lett. A* **315** 162

[54] Kutsyk A M, Kasatkin A L and Kordyuk A A 2021 *Low Temp. Phys.* **47** 920

[55] Lin S Z and Reichhardt C 2013 *Phys. Rev. B* **87** 100508

[56] Mosquera-Polo A S, Aríza-Echeverri E A, Aguirre C, Muñoz-Martínez L F and Faúndez J 2025 *Crystals* **15** 610

[57] Huang Z and Hu X 2016 *J. Supercond. Novel Magn.* **29** 597

[58] Baert M, Metlushko V V, Jonckheere R, Moshchalkov V V and Bruynseraede Y 1995 *Phys. Rev. Lett.* **74** 3269

[59] Simões R P, Venegas P A and Mello D F 2013 *J. Supercond. Nov. Magn.* **26** 2277

[60] Kwok W K, Welp U, Glatz A, Koshelev A E, Kihlstrom K J and Crabtree G W 2016 *Rep. Prog. Phys.* **79** 116501

[61] Blatter G, Feigel'man M V, Geshkenbein V B, Larkin A I and Vinokur V M 1994 *Rev. Mod. Phys.* **66** 1125

[62] Civale L 1997 *Supercond. Sci. Technol.* **10** A11

[63] Brandt E H 1995 *Rep. Prog. Phys.* **58** 1465

[64] Vodolazov D Y and Peeters F M 2007 *Phys. Rev. B* **76** 014521

[65] Villegas J E, Gonzalez E M, Montero M I, Schuller I K and Vicent J L 2003 *Phys. Rev. B* **68** 224504

[66] Reichhardt C, Olson C J and Nori F 1997 *Phys. Rev. Lett.* **78** 2648

[67] Reichhardt C, Olson C J and Grønbech-Jensen N 2000 *Physica C* **341–348** 1081

[68] Aichner B, Mletschnig K L, Müller B, Karrer M, Dosmailov M, Pedarnig J D, Kleiner R, Koelle D and Lang W 2020 *Low Temp. Phys.* **46** 331